

On the Cooper Minimum in Singly ionized and Neutral Argon

O. Hassouneh

Department of Physics, University of Jordan, Amman, 11942, Jordan

N. B. Tyndall, J. Wragg, H. W. van der Hart, and A. C. Brown

Centre for Theoretical Atomic, Molecular and Optical Physics, School of Mathematics and Physics, Queen's University Belfast, Belfast BT7 1NN, United Kingdom

We present an analysis of the appearance of the Cooper Minimum in singly ionized argon in both the photoionization cross-section (PICS) and high-harmonic generation (HHG) spectrum. We employ two computational approaches based on the same R-matrix technique to provide a coherent description of the atomic structure of the Ar^+ system, finding that the PICS and HHG spectrum are affected differently by the inclusion of additional residual ion states and the improved description of correlation effects. Both the PICS and HHG spectrum possess a clear minimum for all atomic structure models used, with the centre of the minimum at 55 eV in the PICS and 60 eV in the HHG spectrum for the most complete description employed. The HHG minimum is systematically shifted to higher energies with respect to the PICS minimum. We also find that the initial magnetic alignment (magnetic quantum number) of the Ar^+ system does not affect substantially the position and shape of the HHG minimum (given a sufficiently detailed atomic structure description), but the harmonic yield is enhanced by two-orders of magnitude for $M_L = 1$ over $M_L = 0$. We also perform similar calculations for neutral argon, finding that this system is more sensitive to enhancements in the atomic structure description.

PACS numbers: 32.80.Rm, 31.15.A-, 42.65.Ky

I. INTRODUCTION

Attosecond physics provides a key window on the fundamental dynamics of atoms [1] and, via the uncertainty relationships, these dynamics are complimentary to atomic structure. This complementarity has recently been investigated in the build up of Fano resonances [2], but is present in other processes. High-harmonic generation (HHG) has long been established as both the source of ultrashort light pulses [3] and a valuable measurement tool in the guise of high-harmonic spectroscopy [4]. The *dynamic* HHG process depends on a *well-timed* photoabsorption process in a short laser pulse. This can be contrasted with a *structure-based* photoionization process, which involves light pulses effectively infinite in extent.

The HHG process has been well described for decades using the simple-man model: an electron is ionized and accelerated by a strong laser field before recolliding with its parent ion and emitting its absorbed energy as a high-energy photon [5]. The simple-man model provides an intuitive classical picture for the process, and describes the gross features of the resulting spectrum of emitted light well, but fails to capture atomic-structure or multi-electron effects [6].

This is particularly troublesome because probing *atomic resonances* with strong-fields has long been a vital function in attosecond physics [6–9]. Certain resonances have been shown to increase the yield of harmonic emission, either in a broad energy range (e.g via the giant resonance in xenon [6, 10]) or at the specific frequencies of the resonances (e.g. via the window resonances in argon [11, 12]) providing important efficiency gains toward attosecond pulse generation.

We have shown previously that HHG at the single-atom level is crucially sensitive to the details of atomic structure of the target system [13, 14] and to the contribution of multiple electrons [15, 16]. One means of addressing the description of multielectron dynamics is to extend traditional methods—based on the single-active-electron approximation—to account for electron correlation via correction terms. Recent attempts at developing such models are strongly suggestive of the crucial role played by multielectron dynamics in determining HHG emission rates, but are unable to provide a quantitative description of HHG yields [17].

The need for an accurate, quantitative description of HHG from rare gas atoms and ions to guide experiment is the motivating factor for several, competing theoretical approaches. Several methods have investigated HHG in the two-electron He atom by solving the fully-dimensional Schrödinger equation [18, 19]. However, such methods are not easily extended to the general multielectron case. One of the most successful approaches for general atoms is the Time Dependent configuration-interaction singles (TDCIS) approach, [10, 20–22]. As the name implies, this method is restricted to the description of singly excited configurations, and the calculations are only applicable to closed-shell systems. In recent years, several other methods have been proposed which offer various advantages for the description of strong-field processes in multi-electron systems [23–28]. Among them, R-matrix with time-dependence (RMT) has emerged as a tractable and flexible approach to general multielectron systems. Crucially, for the present manuscript, RMT affords selectivity in the detail of atomic structure included in calculations, allow-

ing for the description of open-shell systems and multiply excited states.

RMT is thus the leading method able to describe atomic structure in sufficient detail to provide direct, *ab initio* solutions of the time-dependent Schrödinger equation (TDSE) for multielectron atoms or ions. These capabilities have been demonstrated in the investigation of photoionization of Ne^+ in combined infrared/XUV pulses [29]. The approach has recently been used to demonstrate the spin-orbit dynamics in the ground state of carbon with zero and nonzero initial magnetic quantum number [30]. Moreover, the RMT code has been adapted to include a two-electron finite difference outer region to allow the modelling of double-ionization [31–33]. Much recent success in the application of the RMT method has been to compliment and even preempt cutting edge experimental techniques such as attosecond transient absorption spectroscopy [34], high-harmonic spectral caustics [35] and extreme-ultraviolet-initiated high harmonic generation [16, 36].

HHG in ionized noble gas atoms remains a subject of interest for two reasons. Firstly, the highest harmonics generated in HHG from neutral noble gas atoms have been attributed to the presence of singly ionized species [37–39]. And secondly, the role of multiple, closely-spaced ionization thresholds represents a useful analogue for molecular systems. We have previously addressed HHG in singly ionized neon using a previous implementation of RMT, demonstrating the need for the accurate description of multiple ionization thresholds in the process [13]. The equivalent process in singly ionized argon is of enhanced interest because of the Cooper minimum (CM) which we have recently shown to exist in the harmonic spectrum [36]. Such minima are the result of a zero in the matrix element between the d and s continuum waves and the $3p$ -ground state, and have been widely reported for HHG from Ar atoms following their long-established appearance in photoionization spectra [7, 8, 40].

The connection between the CM in the photoionization and HHG spectra has been implicit in many of these previous studies, but no direct comparison has been made because no method allowed for the simultaneous determination of the two. In the present manuscript we present the results of both photoionization and HHG calculations for Ar^+ and investigate therein the appearance of the CM.

II. ATOMIC STRUCTURE DESCRIPTIONS

The overarching theoretical framework for our calculations is the R -matrix approach [41], wherein configuration space is divided into two regions. In an inner region, close to the nucleus, we take full account of multielectron effects, including electron exchange, via a close-coupling with pseudostates expansion. An electron can be ejected into an outer region by ionization and in this region the electron is spatially isolated from the residual ion and

thus exchange can be neglected.

Within the R -matrix paradigm, then, the Ar^+ states are constructed from a single electron and multi-configuration Hartree-Fock (MCHF) orbitals for the residual ion states of Ar^{2+} . The calculation includes all final states with a maximum total angular momentum of 9.

It has been found that there is a strong configuration dependence in the $3s$ and $3p$ orbitals for the ionic states, as well as for the initial $3s^2 3p^5 \ ^2P^o$ bound state for Ar^+ . Thus, we include in our calculations all physical $1s, 2s, 2p, 3s, 3p$ orbitals for the Ar^{2+} description. Furthermore, to improve the description of the Ar^{2+} ion states, and hence the ionization process, we also include pseudo-orbitals $4\bar{s}, 4\bar{p}, 3\bar{d}$ and $4\bar{d}$ to capture short-range correlation effects not well-described by the physical orbitals alone.

If only a single set of orthogonal one-electron orbitals are employed in the calculation, the obtained threshold energy deviates significantly from the corresponding experimental value. Thus, it is necessary to include a large set of doubly-excited configurations to obtain the correct binding energy.

In this work, we employ a “3-state” model, including the three lowest residual ion states— $^3P^e$, $^1D^e$ and $^1S^e$ —determined from two different Ar^{2+} models:

- “3-CI”: including the lowest three CI basis states, whereby, $3s^2 3p^4$, $3s 3p^5$ and $3p^6$ are included in obtaining the wavefunction for each of $^3P^e$, $^1D^e$ and $^1S^e$ residual ion states. In this model we add no correlation orbitals to the system.
- “9-CI”: where we include additional correlation orbitals and allow single and double excitations from the physical $3s, 3p$ orbitals to the $3\bar{d}$ orbital. Hence, in addition to the above, we include all $3s^2 3p^3 3\bar{d}$, $3s 3p^4 3\bar{d}$, $3p^5 3\bar{d}$, $3s^2 3p^2 3\bar{d}^2$, $3s 3p^3 3\bar{d}^2$ and $3p^4 3\bar{d}^2$ CI basis states in determining the wavefunction.

Including double excitations improves the description of the wave functions near the nucleus in the residual ion as well as the interaction between the target and ionized electron at larger distances. This could have an important impact on the description of the ionization process which impacts on both the PICS and the HHG spectrum. The energy spacing between the $^3P^e$ and $^1D^e$ states is within 20% of the experimental value in the 3-CI model and within 5% in the 9-CI model where we allow for doubly-excited states by including more correlation orbitals. The same trend is seen for the $^1S^e$ state (see Tab. I).

In addition, we employ a “5-state” model, in which we include the two higher lying residual ion states of $3s 3p^5 \ ^3P^o$ and $^1P^o$. These higher lying ionization thresholds account for the emission of $3s$ electrons, whereas, the 3-state models allow the emission of $3p$ electrons only. Finally, the “9-state” model includes an additional two $^3P^o$ and two $^1P^o$ ionic target states. The $3s^2 3p^4 \ (^1D^e) nd$

TABLE I: Energies of the three ionization thresholds of Ar^+ with respect to the ground state, as calculated in the present scheme and compared to literature values [42].

Threshold	Energy (eV)		
	Lit.	3-CI	9-CI
$^3P^e$	0.00	0.00	0.00
$^1D^e$	1.73	2.04	1.81
$^1S^e$	4.12	3.31	4.21

states can contain a significant admixture of $3s3p^6$ and when considering emission of a $3s$ electron, we need to take this mixing into account. Although the full interplay cannot be accounted for in a tractable calculation, inclusion of low-lying states may give a first indication of the effects induced by this interaction. This is afforded by the “9-state” model.

For comparison with Ar^+ we also perform a small number of calculations with neutral argon. The atomic structure descriptions chosen follow a similar pattern to Ar^+ . The simplest model, denoted 1S 1-CI (1 state, one configuration) employs only the $3s^23p^5\ ^2P^o$ residual ion state, effectively restricting ionization to the $3p$ orbital (neglecting the inner-valence $3s$ orbital). The largest comprises 8 (two $^2P^e$ and $^2D^e$ and one each of $^2S^e$, $^2P^o$, $^2F^e$, and $^2F^o$) residual ion states, and 8 CI basis (8S 8-CI) states which allow all single- and double-excitations from the physical $3s$ and $3p$ orbitals to the $3d$ orbital. We also employ two models with two residual ion states ($^2P^e$ and $^2S^e$) with 2 CI and 8 CI basis states respectively (2S 2-CI and 2S 8-CI). A complete list of the residual-ion states and configurations used is shown in Tab. II.

HHG spectra are determined from the time-dependent expectation value of the dipole operator as extracted from calculations using the RMT code [43, 44] while photoionization cross sections (PICS) for Ar^+ are extracted from calculations using the Dirac Atomic R-matrix Code (DARC) [45–47]. Calculation of the PICS for neutral argon is performed with the Breit-Pauli (BP) R-matrix codes [47, 48]. These differ from the DARC codes in that they apply relativistic corrections to the Schrödinger equation, whereas the DARC codes solve the Dirac equation. The RMT codes are non-relativistic, but the *same atomic structure description* (atomic orbitals, pseudo-orbitals, configurations) is used as the basis for all calculations performed. Test calculations with a prototype, relativistic RMT code show that the effect of the spin-orbit interaction on the HHG spectra for light species such as Ar and Ar^+ is minimal, even though these effects are important for the *time-independent* calculations with the DARC and BP codes. The use of the R-matrix framework thus allows a direct comparison between the CM in the HHG spectrum and PICS. However, we note that the HHG spectra are resolved into contributions from initial states aligned with $M_L = 0$ and $M_L = 1$, while the PICS is obtained from a mixed initial state.

TABLE II: Atomic structure descriptions for the Ar and Ar^+ models used in the calculations. Model names are derived from the number of residual ion states (S) and the number of configurations (CI) included in the configuration interaction expansion.

Ar^+	
Model	Residual ion states
3S- n CI	$(3s^23p^4)\ ^3P^e, ^1D^e, ^1S^e$
5S- n CI	$(3s^23p^4)\ ^3P^e, ^1D^e, ^1S^e,$ $(3s3p^5)\ ^3P^o, ^1P^o$
9S- n CI	$(3s^23p^4)\ ^3P^e, ^1D^e, ^1S^e,$ $(3s3p^5)\ ^3P^o, ^1P^o,$ $(3s^23p^33d)\ ^3P^o, ^1P^o,$ $(3s^23p^34s)\ ^3P^o, ^1P^o$
Model	Configurations
n S-3CI	$3s^23p^4, 3s3p^5, 3p^6$
n S-9CI	$3s^23p^4, 3s3p^5, 3p^6,$ $3s^23p^33d, 3s3p^43d, 3p^53d,$ $3s^23p^23d^2, 3s3p^33d^2, 3p^43d^2$
Ar	
Model	Residual ion states
1S- n CI	$(3s^23p^5)\ ^2P^o$
2S- n CI	$(3s^23p^5)\ ^2P^o$ $(3s3p^6)\ ^2S^e$
8S- n CI	$(3s^23p^5)\ ^2P^o,$ $(3s3p^6)\ ^2S^e,$ $(3s^23p^53d)\ ^2P^e, ^2D^e, ^2F^e,$ $(3s^23p^54s)\ ^2P^e, ^2D^e,$ $(3s^23p^54p)\ ^2F^o$
Model	Configurations
n S-1CI	$3s^23p^5$
n S-2CI	$3s^23p^5, 3s3p^6$
n S-8CI	$3s^23p^5, 3s3p^6,$ $3s^23p^43d, 3s3p^53d, 3p^63d,$ $3s^23p^33d^2, 3s3p^43d^2, 3p^53d^2$

III. CALCULATION PARAMETERS

For the RMT calculations we employ an 8-cycle, 800 nm laser pulse with a 4-cycle \sin^2 turn-on and turn-off and peak intensity of $4 \times 10^{14} \text{ Wcm}^{-2}$. The pulse is polarized in the z -direction and is spatially homogeneous. The wavefunction is propagated using an Arnoldi propagator of order 8 with a time step of 0.01 a.u.. The

radial wave functions of the inner electrons are expanded on a set of 60 11th order B-splines, using an exponential distribution of knots near the nucleus to near-linear near the boundary with outer-region. This allows for a numerically accurate description both close to, and far away from, the nucleus up to the boundary at $r_{max} = 15$ a.u. The grid spacing in the outer region grid is 0.08 a.u. where the radial wavefunction of the outer electron is expanded on a finite-difference grid out to a radial distance of $2000 a_0$.

As described in ref. [49], using the non-relativistic Lienard-Wiechert potentials in the far field limit, the electric field produced by an accelerated charge is

$$E(t) = k \left\langle \Psi(t) \left| \frac{[p_z, H]}{i\hbar} \right| \Psi(t) \right\rangle + keE_{laser}(t),$$

where $\Psi(t)$ is the time-dependent wavefunction of the system, e is the charge of the electron, z is the polarization axis, k is a constant of proportionality, p_z is the canonical momentum and E_{laser} is the electric field of the laser pulse. Expanding the commutator, we obtain

$$\left\langle \Psi(t) \left| \frac{[p_z, H]}{i\hbar} \right| \Psi(t) \right\rangle = \frac{d}{dt} \langle \Psi(t) | p_z | \Psi(t) \rangle,$$

and it follows that

$$E(t) \propto \ddot{\mathbf{d}}(t) = \frac{d^2}{dt^2} \langle \Psi(t) | \mathbf{z} | \Psi(t) \rangle, \quad (1)$$

where \mathbf{z} is the position operator. Then, the power spectrum of the emitted radiation is given, up to a proportionality constant, by $|\ddot{\mathbf{d}}(\omega)|^2$ - the Fourier transform of $\ddot{\mathbf{d}}(t)$ squared. The dipole acceleration $\ddot{\mathbf{d}}$ cannot however be computed easily (except in simple cases such as atomic helium) as this quantity is prohibitively sensitive to the description of atomic structure at very small radial distances. Instead, the relationships between acceleration, velocity and displacement can be exploited to express the harmonic spectrum in terms of the the dipole velocity and/or length.

Thus in our calculations the harmonic spectrum is calculated from the time-dependent expectation value of the dipole operator \mathbf{D} :

$$\mathbf{d}(t) = \langle \Psi(t) | \mathbf{D} | \Psi(t) \rangle,$$

and of the dipole velocity operator $\dot{\mathbf{D}}$:

$$\dot{\mathbf{d}}(t) = \langle \Psi(t) | \dot{\mathbf{D}} | \Psi(t) \rangle,$$

The harmonic spectrum is then given by

$$S(\omega) = \omega^4 |\mathbf{d}(\omega)|^2 = \omega^2 |\dot{\mathbf{d}}(\omega)|^2,$$

where ω is the photon energy and $\mathbf{d}(\omega)$ and $\dot{\mathbf{d}}(\omega)$ are the Fourier transforms of $\mathbf{d}(t)$ and $\dot{\mathbf{d}}(t)$ respectively. Consistency between the length and velocity form spectra is used as a test of the accuracy of the RMT calculations. For

the largest atomic structure description used we obtain agreement within 20% between the length and velocity form. The spectra shown here are all of the length form, but for all models employed, the comparisons and analysis between HHG spectra apply both to the length and velocity forms.

For the DARC calculations, the R-matrix inner region was set at 13.28 a.u which is just sufficient to encompass the diffuse, $4p$ orbital, and 22 continuum orbitals are used to describe the outgoing electron. An energy mesh of spacing 55 meV was used to scan the photon energy range between 27eV and 160eV. The PICS is calculated in Megabarns ($1 \text{ Mb} = 10^{-18} \text{ cm}^2$) as

$$\sigma = \frac{4\pi a_0^2 \alpha \omega}{3g_i} \sum \langle \Psi_f | \mathbf{D} | \Psi_i \rangle$$

where a_0 is the Bohr radius, α is the fine-structure constant, g_i is the statistical weighting of the initial state and Ψ_i and Ψ_f are the initial and final state wavefunctions respectively. As with the HHG calculations, the PICS can also be calculated using both the length and velocity forms of the dipole operator \mathbf{D} . Up to 45 eV, agreement is found between the two to within 20% and thus all results shown are provided in the length gauge.

IV. RESULTS

A. Singly ionized Argon

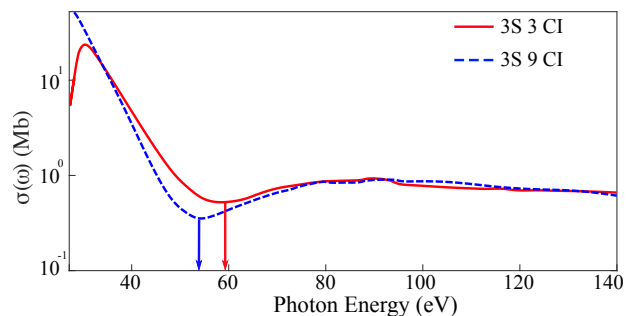


FIG. 1: The calculated total photoionization cross section, σ , of Ar^+ with 3-state/3-CI (solid, red line), and 3-state/9-CI (dashed, blue line) model, as a function of the incident photon energy. The position of the Cooper Minimum is denoted by the vertical lines at 59 eV and 55 eV. The differences between the spectra are around 10% in the high-energy region and 50% around the minimum. The raw data for the figures in this paper can be found via Ref. [50].

Figure 1 shows the photoionization cross section (PICS) of Ar^+ for the 3-state model, with the two different CI bases. For the linearly polarized light pulse here employed, and an initial total magnetic quantum number $M_L = 0$, only $m_l = 0$ electrons will be ejected. Thus, this model allows only for the ejection of a $3p_0$ electron, leaving the residual Ar^{2+} ion in one of the $^3P^e$, $^1D^e$ or $^1S^e$

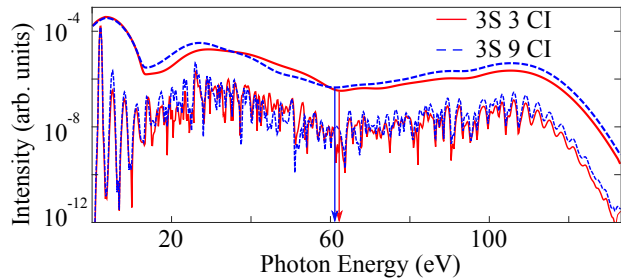


FIG. 2: The calculated harmonic spectrum from Ar^+ at a laser wavelength of 800 nm and peak intensity of $4 \times 10^{14} \text{ W cm}^{-2}$, obtained using the RMT approach for the 3-state/3-CI model (solid, red line) and the 3-state/9-CI (dashed, blue line). The upper lines show the (offset) smoothed spectra which makes clear the slight difference in the positions of the Cooper Minimum, which are denoted by the vertical lines at 64 eV (3S 3-CI) and 62 eV (3S 9-CI). The differences between the spectra are around 40% at the minimum and 60% at the cut-off.

states. The Cooper minimum (CM) is visible in the PICS at 59 eV in the 3-state, 3-CI model. However, the inclusion of doubly-excited configurations in the 9-CI model leads to a shift in the position and shape of the CM, giving a much deeper minimum centred on 55 eV. Measured from the minimum to subsequent maximum, the CM has a depth of 0.40 Mb in the 3-CI case, contrasted with 0.59 Mb for 9-CI. The relative change in the PICS from the additional structure is around 50% at the CM, and 10% at high energy (100 eV).

Figure 2 shows the single-atom harmonic spectrum for Ar^+ generated by a 800 nm pulse, with a peak intensity of $4 \times 10^{14} \text{ W cm}^{-2}$ for the 3-state model, with two different CI bases. As expected, the CM is well replicated in the HHG spectra. At energies below the CM the harmonic yield is slightly suppressed in the 9-CI model, which mirrors the behaviour of the PICS (Fig. 1). However, at slightly higher energies the harmonic yield is higher in the 9-CI case, while the opposite is true for the PICS. Differences in harmonic yield at energies just above the CM may cause a shift in the apparent position of the minimum, which appears at 64 eV for the 3-CI case, but at 62 eV in the 9-CI model. We note that these energies are higher than the corresponding positions in the PICS (59 eV and 54 eV respectively), which is line with previous observations of the CM in neutral argon [7, 8]. However, it is interesting to note that the PICS and HHG spectrum are affected quite differently by the enhanced atomic structure: inclusion of the doubly excited configurations in the 9-CI model has only a small effect on the CM in the HHG spectrum, but changes its position and depth markedly in the PICS.

Additionally, only small differences (10%) are observed at high energy in the PICS, while for the HHG spectra much larger differences (60%) are obtained around the cut-off. This can be explained intuitively: in the PICS the high-energy region is produced by outgoing electrons

escaping the ionic potential with substantial excess energy. In the HHG spectrum, the highest energies are produced by electrons *recolliding* with the ion, and the details of atomic structure are thus more pertinent in the latter case.

Including the $3s3p^5$ residual ion states in the 5-state, 9-CI model allows the emission of the 3s electron. The PICS and HHG spectra obtained from calculations using both the 3-state and 5-state 9-CI models are shown in Fig. 3. Although the shape of the PICS is altered somewhat by the inclusion of the 3s ionization channels, the position of the CM is changed only by 1 eV, and the HHG spectrum is not affected by the 3s electron at all.

That the CM is robust against the action of the 3s electron is to be expected: the CM is caused by the relationship between the $3p$ ground state and the s and d continua. The ionization of Ar^+ should, however, be sensitive to all open ionization channels. This sensitivity is more pronounced in the PICS, as photoionization of the 3s electron by an XUV pulse is substantially more likely than the tunnel-ionization of the 3s in an IR field as required for HHG. Whereas the photoionization yield of 3s at 55 eV is 20% of the $3p$ yield, tunnel ionization of 3s at 800 nm is less than 1% of the $3p$ yield. Thus while the changes in the PICS might be attributed to the influence of the 3s electron, any direct effect on the HHG spectrum should be negligible.

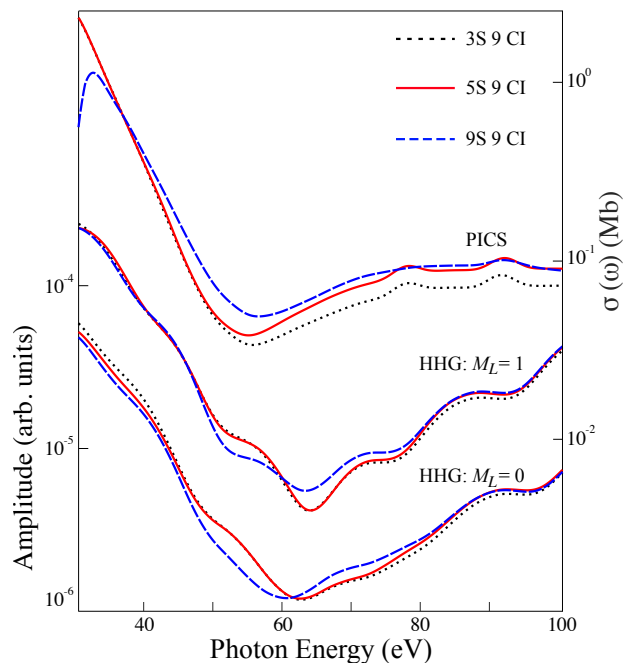


FIG. 3: The photoionization cross section (upper) and smoothed HHG spectrum in an 800 nm, $4 \times 10^{14} \text{ W cm}^{-2}$ field (lower) for Ar^+ as calculated using the 3-state, 9-CI (black, dotted line), 5-state, 9-CI (red, solid line) and 9-state, 9-CI (blue, dashed line) models. The HHG spectrum is shown for an initial total magnetic alignment of $M_L = 1$ (upper) and $M_L = 0$ (lower).

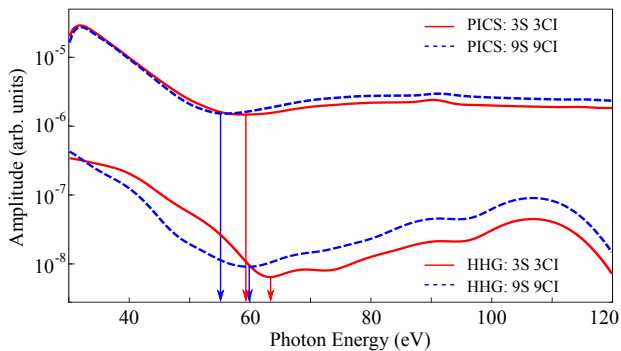


FIG. 4: The photoionization cross section (upper) and smoothed HHG spectrum in an 800 nm, 4×10^{14} Wcm $^{-2}$ field (lower) for Ar $^{+}$ as calculated using both the 3-state, 3-CI (red, solid line) and 9-state, 9-CI (blue, dashed line) models. In each case the position of the Cooper Minimum is denoted by the vertical line

Including the further residual ion states in the 9-state models does, however, illicit more substantial changes in the HHG yield. While the direct effect of these channels on HHG should again be minimal (tunnel-ionization into the additional channels is 1% of the total ionization), the additional structure will have an indirect effect due to enhanced configuration interaction between 3s and 3p emission channels. Changes in the HHG spectrum could be attributed to these indirect effects.

Figure 4 shows the PICS and HHG spectra in both the smallest (3-state, 3-CI) and largest (9-state, 9-CI) models used. The position of the CM is shifted down by 4 eV in both the PICS and HHG spectrum. The enhanced atomic structure description allows a far greater mixing between the 3s and 3p emission channels, which will affect the CM by modifying both the 3p ground state of the Ar $^{2+}$ ion, and the s and p continua of the outgoing or recolliding electron.

All of this implies that the effect of correlation on the dominant 3p ionization channels is substantially more important for HHG than the direct impact of excited residual ion states. The picture for photoionization is not so clear, where both the direct impact of additional ionization channels, and the influence of configuration interaction produce non-negligible changes in the PICS.

We have reported previously that changing the total magnetic quantum number M_L can have a significant effect on HHG from noble-gas ions, including Ar $^{+}$, albeit for shorter wavelengths [13, 15]. Specifically, we have found that for Ar $^{+}$ initially in the $M_L = 0$ state, the HHG yield was reduced by a factor of four compared to $M_L = 1$. For Ne $^{+}$ the effect was even more pronounced—with a factor of 26 difference between the two calculations. Now we assess the effect for an 800 nm laser, allowing us to see the impact on the CM.

Figure 5 shows the HHG spectra for the 9-state, 9-CI model with total magnetic quantum number $M_L = 1$ and $M_L = 0$. The harmonic yield is increased by two

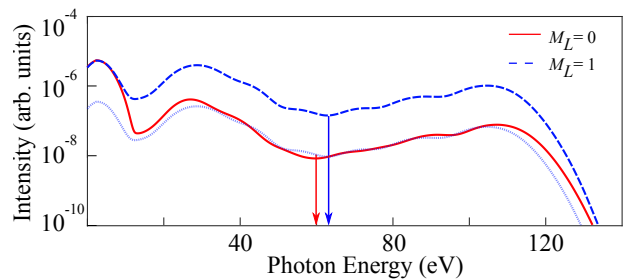


FIG. 5: The calculated harmonic spectrum from Ar $^{+}$ at a laser wavelength of 800 nm and peak intensity of 4×10^{14} W cm $^{-2}$, obtained using the RMT approach for the 3-state/9-CI model with an initial total magnetic alignment of $M_L = 0$ (solid, red line) and $M_L = 1$ (dashed blue line). The Cooper Minimum, is denoted by the vertical lines at 64 ($M_L = 0$) and 63 eV ($M_L = 1$). The renormalised yield for $M_L = 1$ is shown (light blue-dotted line) to demonstrate that the shape of the CM is not affected substantially by the change in magnetic quantum number.

orders of magnitude for $M_L = 1$ over $M_L = 0$: in line with Refs. [13, 15] this reflects an increase in the ionization probability for $M_L = 1$. Despite this substantial increase in yield, the position of the CM is only slightly altered by the change in the magnetic quantum number, appearing at 60 ($M_L = 0$) and 63 eV ($M_L = 1$), and in fact, the shape of the minimum is barely affected at all. The renormalised spectrum for $M_L = 1$ almost exactly overlaps the $M_L = 0$ spectrum in the region of the CM.

B. Neutral Argon

Figure 6 shows the HHG spectra and PICS for neutral argon irradiated by an 8-cycle laser of wavelength of 800 nm and peak intensity 4×10^{14} Wcm $^{-2}$ obtained using the R-matrix approach for the four models described in section II. The CM is present in these spectra between 50 and 65 eV and— as was observed for singly-ionized argon— is shifted systematically to higher energies in the HHG spectra relative to the PICS. The inclusion of additional atomic structure causes the position of the minimum to shift to lower energies for both the HHG spectra and PICS, and adding extra residual ion states is seemingly less important than the accurate description of electron correlation which is afforded by the inclusion of more configuration interaction terms. This is reflected in the fact that the position and shape of the minimum changes quite sharply between the 2S 2-CI and 2S 8-CI calculations, but does not change substantially between the 2S 8-CI and 8S 8-CI calculations.

Again, we expect the direct effect of the 3s electron to be minimal— tunnel ionization of the 3p electron outweighs that of the 3s by a factor of 10^6 — and yet the changes wrought by the 3s electron's inclusion in both the HHG spectra and PICS are clearly visible. We can thus attribute this effect to the indirect effect of corre-

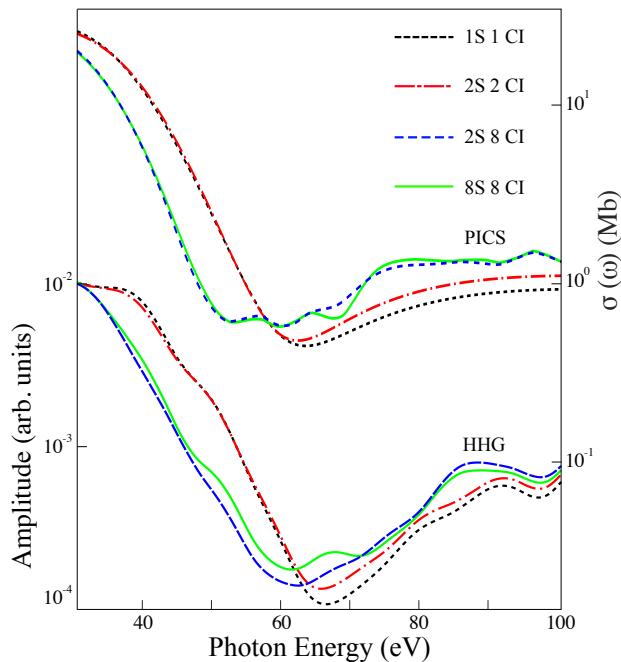


FIG. 6: The photoionization cross section (upper) and smoothed HHG spectrum in an 800 nm, 4×10^{14} Wcm $^{-2}$ field (lower) for Ar obtained using the R-matrix approach with the 1-state 1-CI (black dotted line), 2-state 2-CI (red dot-dashed line), 2-state 2-CI (blue dashed line) and 8-state 8-CI (green solid line) models.

lation between outgoing electron emission channels. Finally, comparing Fig. 6 with Fig. 4 it is noticeable that the inclusion of additional atomic structure has a greater effect on the appearance of the CM in neutral Ar than in Ar $^{+}$.

V. ANALYSIS

Table III shows a summary of the position of the Cooper Minimum for the various calculations performed in this work. For Ar $^{+}$ the position of the CM in the HHG spectrum is systematically higher than in the PICS, and while the gap ranges from 5 eV (3S 9-CI) to 8 eV (5S 3-CI) the most complete atomic structure description leads to a gap of 5 eV. For Ar this gap is 10 eV. This is in line with previous studies of Cooper Minima in other systems— e.g. experimental measurements in krypton show a shift of the CM in HHG to higher energies than the PICS[6]. However, neutral Ar is a better known case, and some literature values for the position of the CM in Ar are shown in the table. (We do observe a systematic shift to higher energies in our results with respect to the literature values, but note that the relative differences between the PICS and HHG spectra are consistent with our results) Higuete *et al* found shifts from 50 eV to 54 eV (theory) 49 eV to 54 eV (experiment) between the PICS and HHG minima [8]. However, these

TABLE III: The position of the Cooper Minimum in Ar $^{+}$ and Ar in both the PICS and HHG spectrum. The atomic structure descriptors denote the number of residual ion states (S) and the number of configurations in the configuration interaction (CI) description. The literature values for the PICS and HHG CM in Ar are shown for comparison and are taken from ref. [51] and refs. [7, 8] respectively.

Atomic Structure	PICS (eV)	HHG (eV)	
		$M_L = 0$	$M_L = 1$
Ar $^{+}$			
3S 3-CI	59	64	63
3S 9-CI	55	62	64
5S 3-CI	56	62	63
5S 9-CI	54	62	64
9S 9-CI	55	60	63
Ar			
1S 1-CI	63	66	-
2S 2-CI	62	65	-
2S 8-CI	53	61	-
8S 8-CI	52	62	-
Lit.	48	54	-

differences could not be trivially explained by the small difference (2 eV) between the position of the minimum in the photoionization and photorecombination dipoles.

In the present work however, we can venture some ideas regarding the difference in the appearance of the CM based on the different atomic structure descriptions employed in our calculations. Clearly an improvement in the atomic structure description does not eradicate the shift and nor should we expect it to, as the shift is reported (for Ar at least) in various experimental works [7, 8]. Neither do the PICS and HHG spectra respond uniformly to changes in the atomic structure description— as noted above and as is visible from Tab. III. For Ar $^{+}$ the inclusion of additional, 3s ionization thresholds has a direct impact on the shape of the CM in the PICS, but not in HHG, while the enhanced description of correlation effects, both via the inclusion of additional configurations and residual ion states, has a similarly marked effect on both the PICS and HHG spectra. For Ar the situation is similar, although the inclusion of the 3s ionization thresholds has even less of an effect than for Ar $^{+}$.

In some sense, this is to be expected— the HHG spectrum is generated by a strong field, i.e. is mediated by low energy photons. This will bias the mechanism towards the ionization of more weakly bound electrons. By contrast, the PICS is mediated by high energy photons, which can more easily liberate the inner-valence electrons. Thus, in the Ar or Ar $^{+}$ picture, the ionization of the 3s electrons will be more important in the photoionization process than in the HHG process. Correspondingly, the inclusion of additional residual ion states, which allow a better description of the ionization of the 3s electrons, will have a more substantial influence on

the shape of the PICS than the HHG spectrum.

By contrast the inclusion of additional residual ion configurations (i.e. the improved description of electron correlation) affects the PICS and HHG spectrum similarly, shifting the CM position from 59 eV to 55 eV and 64 eV to 60 eV respectively in Ar^+ . Furthermore, Fig. 6 shows that the same qualitative change in the shape of the minimum is effected by the inclusion of these effects in Ar.

Naive models of HHG might neglect all but the ground state target system, which we have shown previously to have a profound impact on the resulting HHG yield [11, 14]. Here we have demonstrated that even in strong, long-wavelength laser fields, the details of atomic structure, and correlation in particular, can influence the appearance of important resonant structures such as the Cooper Minimum.

VI. CONCLUSION

The appearance of the Cooper Minimum in high-harmonic spectra has long been used as a test case for the theoretical connection between the mechanisms of photoionization and HHG [6, 8]. However, until recently, the capability to describe atomic processes in strong-fields with an accurate description of electron correlation was computationally intractable, and thus a single study addressing both mechanisms in suitable detail has been elusive. In this paper we have performed a systematic analysis of the effects of the atomic structure description on the appearance of the CM in singly-ionized argon in both the PICS and HHG spectrum, finding that each process is sensitive to slightly different details of the description. Photoionization is more sensitive to the description of the residual ion states (i.e. the accurate description of multiple ionization pathways), whereas HHG is affected more by the details of the electron correlation.

We find, in concert with studies in other systems, that the CM appears at lower energies in the PICS than in the HHG spectrum. For the most complete description used the CM appears at an energy of 55 eV in the PICS and

60 eV in the HHG spectrum in Ar^+ and 52 eV and 62 eV in Ar. We also note that the total magnetic quantum number has a negligible effect on the position and shape of the CM in Ar^+ , despite a two-orders-of-magnitude increase in the harmonic yield for $M_L = 1$ over $M_L = 0$.

What may seem like insignificant differences in the spectra may in fact become very important as the attosecond tool-set expands and provides ever more accurate resolution of atomic structure effects. We have recently reported on XUV initiated HHG [16], which offers the possibility of stimulating electron correlation effects with multicolor laser schema (rather than searching for their ‘natural’ appearance in single-color HHG spectra). In such scenarios the accurate, time-dependent description of electron-correlation will be absolutely necessary to analyze experimentally produced spectra and to guide the development of the theory of attosecond dynamics. To this end, ongoing development of the R-matrix with time-dependence method will afford capability to investigate spin-orbit induced dynamics, the interaction of atomic or ionic systems with arbitrarily polarised laser pulses, and time-dependent modelling of molecular systems, all of which are predicated on the ability to describe atomic (molecular) structure and correlation effects accurately, and resolve their effects on experimentally observable quantities, as we have done in this paper.

VII. ACKNOWLEDGEMENTS

HWvdH and ACB acknowledge financial support from EPSRC, under Grants No. EP/P013953/1 and EP/P022146/1. OH acknowledges support from The Deanship of Academic Research and Quality Assurance at the University of Jordan. This work relied on the ARCHER UK National Supercomputing Service (www.archer.ac.uk). The data presented in this paper may be found at Ref. [50]. The RMT code is part of the UK-AMOR suite, and can be obtained for free from Ref. [52].

-
- [1] P. B. Corkum and F. Krausz, Attosecond science, *Nat. Phys.* **3**, 381 (2007).
 - [2] A. Kaldun, *et al.*, Observing the ultrafast buildup of a fano resonance in the time domain, *Science* **354**, 738 (2016).
 - [3] T. Gaumnitz, *et al.*, Streaking of 43-attosecond soft-X-ray pulses generated by a passively CEP-stable mid-infrared driver, *Opt. Express* **25**, 27506 (2017).
 - [4] O. Smirnova and O. Gessner, Attosecond spectroscopy, *Chem. Phys.* **414**, 1 (2013).
 - [5] P. B. Corkum, Plasma perspective on strong field multiphoton ionization, *Phys. Rev. Lett.* **71**, 1994 (1993).
 - [6] A. D. Shiner, *et al.*, Probing collective multi-electron dynamics in xenon with high-harmonic spectroscopy, *Nat. Phys.* **7**, 464 (2011).
 - [7] H. J. Wörner, H. Niikura, J. B. Bertrand, P. B. Corkum, and D. M. Villeneuve, Observation of electronic structure minima in high-harmonic generation, *Phys. Rev. Lett.* **102**, 103901 (2009).
 - [8] J. Higuette, *et al.*, High-order harmonic spectroscopy of the Cooper minimum in argon: experimental and theoretical study, *Phys. Rev. A* **83**, 053401 (2011).
 - [9] A. D. Shiner, *et al.*, Observation of cooper minimum in krypton using high harmonic spectroscopy, *J. Phys. B: At., Mol. Opt. Phys.* **45**, 074010 (2012).
 - [10] S. Pabst and R. Santra, Strong-field many-body physics and the giant enhancement in the high-harmonic spectrum of xenon, *Phys. Rev. Lett.* **111**, 233005 (2013).
 - [11] A. C. Brown, S. Hutchinson, M. A. Lysaght, and H. W. van der Hart, Interference between competing pathways

- in atomic harmonic generation, *Phys. Rev. Lett.* **108**, 063006 (2012).
- [12] J. Rothhardt, *et al.*, Enhancing the macroscopic yield of narrow-band high-order harmonic generation by Fano resonances, *Phys. Rev. Lett.* **112**, 233002 (2014).
- [13] O. Hassouneh, A. C. Brown, and H. W. van der Hart, Multichannel interference in high-order-harmonic generation from Ne^+ driven by an ultrashort intense laser pulse, *Phys. Rev. A* **89**, 033409 (2014).
- [14] A. C. Brown and H. W. van der Hart, Influence of multiple ionization thresholds on harmonic generation from Ar^+ , *Phys. Rev. A* **86**, 063416 (2012).
- [15] A. C. Brown and H. W. van der Hart, Enhanced harmonic generation from Ar^+ aligned with $M = 1$, *Phys. Rev. A* **88**, 033419 (2013).
- [16] A. C. Brown and H. W. van der Hart, Extreme-ultraviolet-initiated high-order harmonic generation: Driving inner-valence electrons using below-threshold-energy extreme-ultraviolet light, *Phys. Rev. Lett.* **117**, 093201 (2016).
- [17] A. Gordon, F. X. Kärtner, N. Rohringer, and R. Santra, Role of many-electron dynamics in high harmonic generation, *Phys. Rev. Lett.* **96**, 223902 (2006).
- [18] J. S. Parker, *et al.*, High-energy cutoff in the spectrum of strong-field nonsequential double ionization, *Phys. Rev. Lett.* **96**, 133001 (2006).
- [19] J. M. Ngoko Djiokap and A. F. Starace, Evidence of the $2s2p(^1P)$ doubly excited state in the harmonic generation spectrum of helium, *Phys. Rev. A* **84**, 013404 (2011).
- [20] L. Greenman, *et al.*, Implementation of the time-dependent configuration-interaction singles method for atomic strong-field processes, *Phys. Rev. A* **82**, 023406 (2010).
- [21] S. Pabst and R. Santra, Spin-orbit effects in atomic high-harmonic generation, *J. Phys. B: At. Mol. Phys.* **47**, 124026 (2014).
- [22] S. Pabst, L. Greenman, D. A. Mazziotti, and R. Santra, Impact of multichannel and multipole effects on the Cooper minimum in the high-order-harmonic spectrum of argon, *Phys. Rev. A* **85**, 023411 (2012).
- [23] L. Torlina and O. Smirnova, Time-dependent analytical R -matrix approach for strong-field dynamics. i. one-electron systems, *Phys. Rev. A* **86**, 043408 (2012).
- [24] L. Torlina, M. Ivanov, Z. B. Walters, and O. Smirnova, Time-dependent analytical R -matrix approach for strong-field dynamics. ii. many-electron systems, *Phys. Rev. A* **86**, 043409 (2012).
- [25] T. Sato and K. L. Ishikawa, Time-dependent complete-active-space self-consistent-field method for multielectron dynamics in intense laser fields, *Phys. Rev. A* **88**, 023402 (2013).
- [26] H. Miyagi and L. B. Madsen, Time-dependent restricted-active-space self-consistent-field theory for laser-driven many-electron dynamics, *Phys. Rev. A* **87**, 062511 (2013).
- [27] D. Hochstuhl and M. Bonitz, Time-dependent restricted-active-space configuration-interaction method for the photoionization of many-electron atoms, *Phys. Rev. A* **86**, 053424 (2012).
- [28] H. Miyagi and L. Bojer Madsen, Time-dependent restricted-active-space self-consistent-field singles method for many-electron dynamics, *J. Chem. Phys.* **140**, (2014).
- [29] H. W. van der Hart and R. Morgan, Population trapping in bound states during IR-assisted ultrafast photoionization of Ne^+ , *Phys. Rev. A* **90**, 013424 (2014).
- [30] H. F. Rey and H. W. van der Hart, Probing spin-orbit-interaction-induced electron dynamics in the carbon atom by multiphoton ionization, *Phys. Rev. A* **90**, 033402 (2014).
- [31] J. Wragg, J. S. Parker, and H. W. van der Hart, Double ionization in R -matrix theory using a two-electron outer region, *Phys. Rev. A* **92**, 022504 (2015).
- [32] J. Wragg and H. W. van der Hart, Spin and spatial dynamics in electron-impact scattering off S -wave He using R -matrix-with-time-dependence theory, *Phys. Rev. A* **94**, 032706 (2016).
- [33] H. W. van der Hart, Time-dependent R -matrix theory applied to two-photon double ionization of He, *Phys. Rev. A* **89**, 053407 (2014).
- [34] T. Ding, *et al.*, Time-resolved four-wave-mixing spectroscopy for inner-valence transitions, *Opt. Lett.* **41**, 709 (2016).
- [35] K. R. Hamilton, H. W. van der Hart, and A. C. Brown, Pulse-shape control of two-color interference in high-order-harmonic generation, *Phys. Rev. A* **95**, 013408 (2017).
- [36] D. D. A. Clarke, H. W. van der Hart, and A. C. Brown, Extreme-ultraviolet-initiated high-order harmonic generation in Ar^+ , *Phys. Rev. A* **97**, 023413 (2018).
- [37] M. Zepf, B. Dromey, M. Landreman, P. Foster, and S. M. Hooker, Bright quasi-phase-matched soft-X-ray harmonic radiation from argon ions, *Phys. Rev. Lett.* **99**, 143901 (2007).
- [38] C.-G. Wahlström, *et al.*, High-order harmonic generation in rare gases with an intense short-pulse laser, *Phys. Rev. A* **48**, 4709 (1993).
- [39] E. A. Gibson, *et al.*, High-order harmonic generation up to 250 eV from highly ionized argon, *Phys. Rev. Lett.* **92**, 033001 (2004).
- [40] J. W. Cooper, Photoionization from outer atomic subshells. a model study, *Phys. Rev.* **128**, 681 (1962).
- [41] P. G. Burke, *R-matrix Theory of Atomic Collisions* (Springer Berlin Heidelberg, 2011).
- [42] A. E. Kramida, Y. Ralchenko, J. Reader, and N. A. Team, NIST atomic spectra database, (ver 5.5.2) (2018), URL <http://physics.nist.gov/asd>.
- [43] L. R. Moore, *et al.*, The RMT method for many-electron atomic systems in intense short-pulse laser light, *J. Mod. Optics* **58**, 1132 (2011).
- [44] O. Hassouneh, A. C. Brown, and H. W. van der Hart, Harmonic generation by noble-gas atoms in the near-IR regime using ab initio time-dependent R -matrix theory, *Phys. Rev. A* **90**, 043418 (2014).
- [45] N. B. Tyndall, C. A. Ramsbottom, C. P. Ballance, and A. Hibbert, Valence and L-shell photoionization of Cl-like argon using R-matrix techniques, *MNRAS* **456**, 366 (2016).
- [46] P. H. Norrington and I. P. Grant, Low-energy electron scattering by Fe XXIII and Fe VII using the Dirac R -matrix method, *J. Phys. B: At. Mol. Phys.* **20**, 4869 (1987).
- [47] C. Ballance, Parallel R-matrix codes (2018), URL <http://connorb.freeshell.org>.
- [48] N. S. Scott and P. G. Burke, Electron scattering by atoms and ions using the Breit-Pauli Hamiltonian: an R-matrix approach, *J. Phys. B: At. Mol. Phys.* **13**, 4299 (1980).
- [49] A. C. Brown, D. J. Robinson, and H. W. van der Hart,

Atomic harmonic generation in time-dependent R-matrix theory, *Phys. Rev. A* **86**, 053420 (2012).

[50] A. C. Brown, Cooper minimum in PICS and HHG spectra in Ar⁺, *PURE research database* (2018).

[51] J. A. R. Samson and W. C. Stolte, Precision measurements of the total photoionization cross-sections of He,

Ne, Ar, Kr, and Xe, *J. Electron Spec. Relat. Phen.* **123**, 265 (2002).

[52] The RMT code (2018), URL <https://gitlab.com/Uk-amor/RMT/rmt>.